npj | parkinson's disease

Article

Published in partnership with the Parkinson's Foundation

https://doi.org/10.1038/s41531-026-01263-5

Inhibition of de novo ceramide synthesis mitigates alpha-synuclein pathology in a Parkinson's disease mouse model

Eunkyung Lee[1,2], Moon-young Park[1], Minkuk Park[3], Na-Yeong Kim[1], Shibo Wei[1], Nahee Hwang[4], Dongryeol Ryu[1], Hoon Ryu[2], Dohyun Park[1] ✉, Gakyung Lee[3] ✉ & Chang-Myung Oh[1] ✉

Parkinson's disease (PD) is a progressive neurodegenerative disorder characterized by the loss of dopaminergic neurons and the accumulation of α-synuclein aggregates. Ceramide metabolism is increasingly implicated in protein aggregation and mitochondrial dysfunction, both of which are prevalent in neurodegenerative disorders. While prior studies using cell lines have hinted at ceramide's role in PD, the in vivo relevance and therapeutic efficacy of inhibiting its synthesis remained largely unexplored. We aimed to evaluate the therapeutic potential of inhibiting ceramide synthesis in various models of PD, including the A53T α-synuclein transgenic mouse model, primary neurons from patients with PD, and patient-derived midbrain organoids. We found that inhibiting de novo ceramide biosynthesis decreases α-synuclein aggregation and improves motor and cognitive function in A53T α-synuclein transgenic mice. Treatment with myriocin, a serine palmitoyltransferase inhibitor, restored mitochondrial morphology, enhanced mitophagy, and reduced neuroinflammation. Single-nucleus transcriptomic analysis revealed that myriocin normalized gene networks related to synaptic transmission, mitochondrial homeostasis, and inflammation. Additionally, human midbrain organoids derived from PD patient-induced pluripotent stem cells exhibited reduced α-synuclein aggregation and preserved dopaminergic neurons following myriocin treatment. Together, these results suggest that targeting ceramide synthesis is a promising strategy for addressing protein aggregation and neuronal death in PD.

Parkinson's disease (PD) is the second most common neurodegenerative disorder, characterized by progressive motor dysfunction and the formation of Lewy bodies, which contain aggregated α-synuclein, within dopaminergic neurons of the substantia nigra[1]. The etiology of PD is multifaceted, involving α-synuclein aggregation and mitochondrial dysfunction in neurodegeneration as central pathogenic pillars, though the precise molecular triggers remain incompletely understood[1,2]. Despite considerable research, current treatments only offer symptomatic relief and fail to halt underlying neurodegeneration[3,4], highlighting the urgent need for disease-modifying therapies.

Ceramides are bioactive lipids that serve as structural components and key signaling molecules in processes, including apoptosis, autophagy, and inflammation[5,6]. Emerging evidence has cast a spotlight on sphingolipid metabolism, particularly ceramide homeostasis, in the broader context of neurodegenerative diseases and age-related pathologies[7,6]. Ceramide accumulation exacerbates mitochondrial dysfunction, protein aggregation, and neuroinflammation, thereby contributing to disease progression[6]. Previous studies using cellular models, such as SH-SY5Y neuroblastoma cells, have indicated that ceramide accumulation can drive α-synuclein-related pathology and mitochondrial impairment[8,9]. Similar mechanisms involving ceramide-induced disruption of proteostasis and mitochondrial function have been identified in age-related declines in other tissues, such as skeletal muscle, where the inhibition of de novo ceramide synthesis restored mitochondrial function and protein homeostasis[10,11].

In this study, we aimed to evaluate the therapeutic potential of ceramide synthesis inhibition in various PD models, including the A53T α-

[1]Department of Biomedical Science and Engineering, Gwangju Institute of Science and Technology, Gwangju, Korea. [2]Center for Brain Disorders, Brain Science Institute, Korea Institute of Science and Technology (KIST), Seoul, Republic of Korea. [3]Department of Integrative Biological Sciences and Industry, Sejong University, Seoul, Republic of Korea. [4]Department of Biomedical Sciences, Yonsei University College of Medicine, Seoul, Korea. ✉e-mail: dohyun3.park@samsung.com; lgg1025@sejong.ac.kr; cmoh@gist.ac.kr

synuclein transgenic mouse (A53T mouse) model, primary neurons from patients with PD, and patient-derived midbrain organoids. We employed single-nucleus RNA sequencing (snRNA-seq), lipidomics, histological analysis, and behavioral assessments to comprehensively investigate the impact of ceramide inhibition on PD pathology.

Results

Elevated ceramide levels and biosynthesis genes in Parkinson's disease brains and dopaminergic neurons

To elucidate the involvement of ceramide metabolism in PD pathology, we measured ceramide levels in postmortem midbrain tissue samples, categorizing the analysis based on the presence or absence of Lewy bodies, a pathological hallmark associated with synucleinopathies such as PD and Lewy body dementia (LBD)[12]. Using mass spectrometry, we identified significant elevations of 19 ceramide species in midbrain tissues from patients with LBD ($n = 6$) compared to healthy controls ($n = 6$) (Fig. 1a). Among these, ceramide species containing long-chain acyl groups showed a significant increase in LBD brains compared to controls. These findings suggest an association between ceramide accumulation and synucleinopathy-related neurodegeneration. Further studies are needed to establish a direct link with Lewy body pathology.

Next, to investigate alterations in ceramide metabolism associated with PD pathogenesis, we analyzed snRNA-seq data obtained from the Gene Expression Omnibus (GEO) database. Specifically, we compared transcriptomic changes in midbrain dopaminergic neurons between PD patients and controls (GSE accession number: 243639). Using unbiased clustering, we identified six subtypes in neuron cluster (Fig. 1b; Supplementary Fig. 1a). Among these six neuron subtypes, cluster_0 displayed expression of specific genes associated with dopaminergic neurons, including tyrosine hydroxylase (TH) and solute carrier family 6 member 3 (*SLC6A3*)[13] (Fig. 1c). Then, we analyzed differentially expressed genes (DEGs) in dopaminergic neurons (cluster_0) between patients with PD and controls. The volcano plot comparing PD and control samples showed significant DEGs in dopaminergic neurons. Inflammatory response-related genes, including C-C motif ligand 3-like 1 (*CCL3L1*)[14], connexin 43 (*GJA1*)[15], and alpha-2-glycoprotein 1, zinc-binding (*AZGP1*)[16] were increased. In contrast, genes related to dopamine signaling Ras Like Without CAAX 2 (*RIT2*)[17] were decreased (Supplementary Fig. 1b).

The Z-score normalized expression profiles of DEGs revealed a significant upregulation of key enzymes involved in ceramide biosynthesis and metabolism, including ceramide synthase 5 (*CERS5*), *CERS6*, dihydroceramide desaturase 1 (*DEGS*), and glucocerebrosidase (*GBA*) in dopaminergic neurons from patients with PD compared to controls (Fig. 1d). Additionally, other key enzymes implicated in ceramide metabolism which have shown associations with PD, including acid ceramidase (*ASAH1*) and ceramide kinase (*CERK*), were also differentially expressed[18]. These findings suggest a perturbed ceramide homeostasis in the midbrain region of PD patients, potentially contributing to disease pathogenesis. Notably, we observed increased expression of ASAH1 and GBA1. These transcriptional changes are likely to be compensatory responses to substrate accumulation or lysosomal dysfunction, rather than primary pathogenic mechanisms. Further studies in human tissue are required to confirm these findings.

Furthermore, we observed significant downregulation of genes associated with the mitophagy pathway in dopaminergic neurons from patients with PD compared to controls (Supplementary Fig. 1c). We further validated this disruption in ceramide homeostasis using another public transcriptomic dataset from human PD brains (GSE accession number: 156776). In this dataset, we identified 22 distinct cell subtypes with notable upregulation of genes related to ceramide biosynthesis in astrocytes and oligodendrocytes (Fig. 1e and Supplementary Fig. 1d). The DA_OL_2 cells, a subtype of oligodendrocytes, exhibited increased expression of ceramide pathway genes including *CERS1, CERs2* and *CERS4*, as revealed by gene ontology analysis (Fig. 1f and Supplementary Fig. 1e, f). These results suggest that dysregulated ceramide metabolism, particularly within specific neuronal and glial subtypes, also contributes to the pathogenic mechanisms underlying PD.

Inhibiting ceramide synthesis reduces the aggregation of α-synuclein through enhanced mitophagy in human neuroblastoma cells

A previous study demonstrated that inhibiting de novo ceramide synthesis—either through genetic depletion of serine palmitoyltransferase long chain base subunit 1 (SPTLC1) or pharmacological inhibition of SPT using myriocin—effectively mitigates proteotoxic stress by restoring mitochondrial homeostasis in aged skeletal muscle[10]. To investigate whether ceramide depletion can diminish α-synuclein-induced proteotoxicity in neuronal cells, we suppressed ceramide synthesis in a cellular model expressing aggregation-prone α-synuclein through both genetic and pharmacological approaches. We specifically employed SH-SY5Y cells that stably overexpress the pathogenic A53T α-synuclein mutant (A53T-SY5Y cells)[19]. Genetic silencing of SPTLC1 in these cells significantly reduced α-synuclein aggregation (Fig. 2a and Supplementary Fig. 1g). Consistent with this finding, Western blot analysis confirmed decreased levels of insoluble α-synuclein following SPTLC1 knockdown (Fig. 2b). Concomitantly, molecular markers indicative of enhanced mitophagic flux were significantly upregulated, as evidenced by increased phosphorylation of parkin and elevated levels of LC3-II following SPTLC1 silencing in the A53T-SY5Y cells (Fig. 2c). Parkin protein levels were reduced in A53T-SY5Y cells compared to controls, consistent with previous reports showing α-synuclein-mediated Parkin depletion in neuronal models[20]. Silencing of SPTLC1 restored Parkin levels in A53T-SY5Y cells, suggesting that ceramide accumulation contributes to Parkin degradation (Fig. 2c). Furthermore, increased protein ubiquitination indicates enhanced clearance of aggregated proteins (Fig. 2d and Supplementary Fig. 1h). Similarly, pharmacological inhibition of SPT with myriocin resulted in decreased α-synuclein aggregation (Fig. 2e, f and Supplementary Fig. 1i, j) and increased markers of mitophagy and ubiquitination levels (Fig. 2g, h). Collectively, these findings indicate that inhibition of ceramide synthesis mitigates α-synuclein proteotoxicity by activating mitophagy and improving protein clearance mechanisms.

Myriocin treatment reduces α-synuclein pathology in a PD mouse model

To evaluate the therapeutic potential of ceramide synthesis inhibition in vivo, we employed a transgenic mouse model of PD that expresses the aggregation-prone human α-synuclein mutant A53T (line M83, A53T mice)[21]. These mice develop progressive motor impairment, α-synuclein aggregation, and neurodegeneration, thus recapitulating hallmark characteristics of PD[21]. Initiation of the intervention at 5 months of age involved treatment with myriocin (0.4 mg/kg) or a vehicle control, administered intraperitoneally three times weekly for either 5 months (E1) or 7 months (E2) (Fig. 3a). Myriocin administration significantly reduced ceramide levels in plasma (Fig. 3b), midbrain (Fig. 3c), and hippocampus (Supplementary Fig. 2a–d). Behavioral evaluations using open field testing revealed significant deficits in A53T mice treated with vehicles compared to wild-type (WT) controls. These deficits were characterized by decreased exploration of the central zone and reduced total distance traveled, indicative of anxiety-like behavior and impaired locomotion, respectively. Although myriocin treatment did not significantly change entries or time spent in the center zone, it significantly improved total distance traveled, indicating enhanced motor activity (Fig. 3d, e). Additionally, the Y-maze spontaneous alternation test revealed impaired spatial working memory in vehicle-treated A53T mice, as indicated by a lower spontaneous alternation percentage compared to WT controls. Myriocin-treated mice exhibited significantly improved performance on this test, suggesting a restoration of cognitive function (Fig. 3f).

Next, we examined the effects of myriocin treatment on neurodegeneration and α-synuclein aggregation in A53T mice. Immunohistochemical analysis of TH, a marker of dopaminergic neurons, revealed a significant

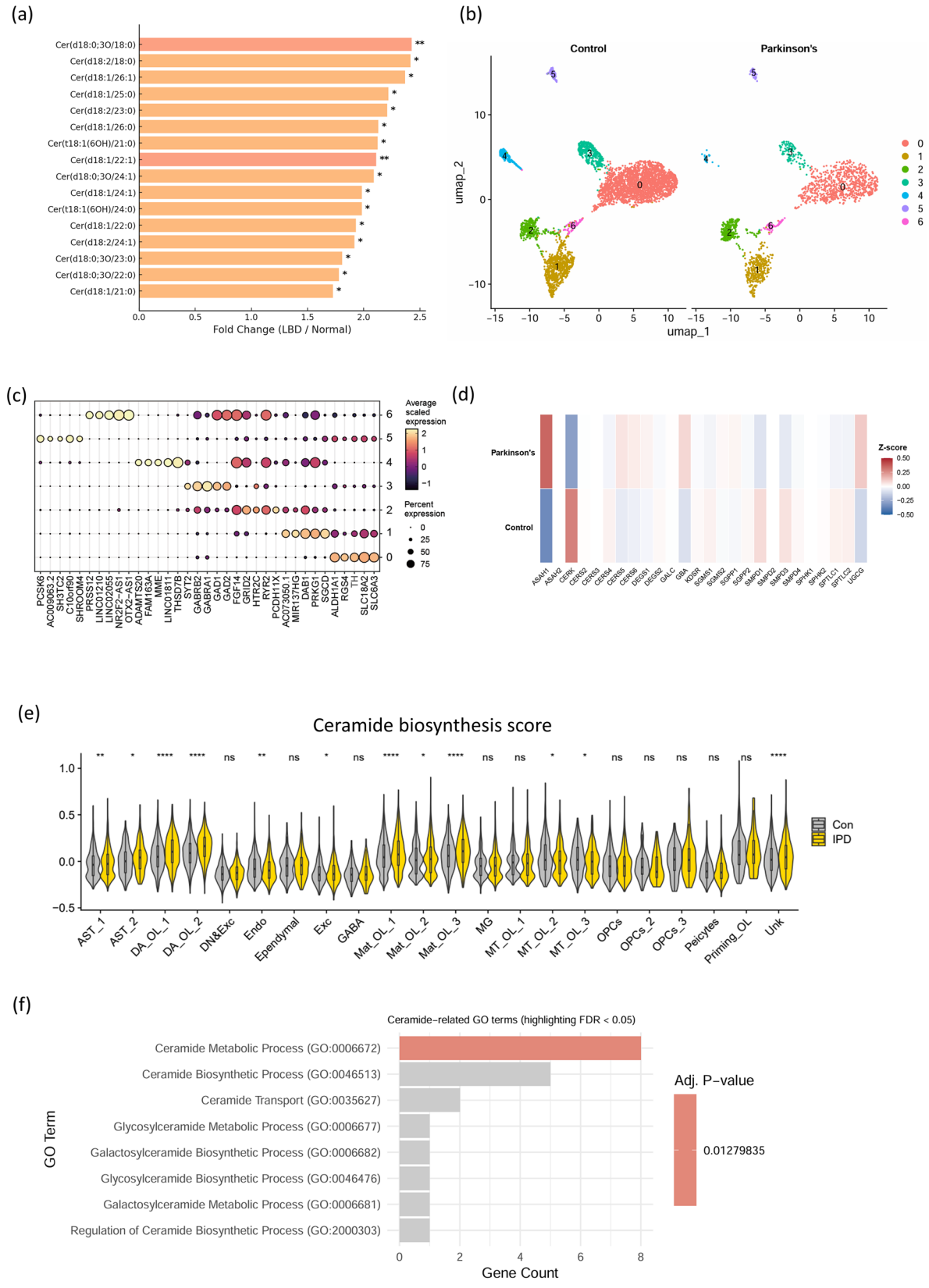

loss of TH-positive neurons in the substantia nigra pars compacta (SNc) and ventral tegmental area (VTA) of vehicle-treated A53T mice compared to WT controls. Myriocin treatment substantially ameliorated this neuronal loss, indicating that inhibition of ceramide synthesis confers neuroprotection within this PD model (Fig. 3g and Supplementary Fig. 2e).

Thioflavin T staining, utilized for the identification of protein aggregates, revealed decreased aggregation in myriocin-treated mice compared to vehicle controls (Supplementary Fig. 2f). In addition, immunofluorescence staining for phosphorylated α-synuclein (p-α-synuclein, Ser129), a hallmark of pathological α-synuclein aggregates, revealed significant accumulation in

Fig. 1 | Elevated ceramide levels and increased expression of ceramide biosynthetic genes in Parkinson's disease (PD) brains. a Quantification of ceramide species in postmortem midbrain tissues from individuals with Lewy body dimentia (LBD; $n = 6$) and age-matched neurologically healthy controls ($n = 6$) using targeted UHPLC-MS/MS. Bar graph shows ceramide species significantly increased in LBD tissue compared to control tissue (fold-change > 1.5; FDR-adjusted $p < 0.05$). Long-chain acyl ceramides (e.g., C16:0, C18:0, C22:0, C27:0) were among the most elevated in LBD brains. **b** UMAP visualization of single-nucleus RNA-seq data (GSE243639) from midbrain samples of PD patients and controls. Unsupervised clustering identified multiple neuronal and non-neuronal subpopulations. Cluster identity is color-coded. **c** Dot plot showing the expression of canonical neuronal markers across neuronal subtypes. Dopaminergic neuron identity was assigned to cluster_0 based on high expression of *TH* and *SLC6A3*. **d** Heatmap displaying Z-score standardized expression of ceramide biosynthesis and metabolism genes in dopaminergic neurons from Parkinson's disease (PD) patients and healthy controls. Each gene's expression was standardized across groups to highlight relative differences. Visual inspection suggests higher expression of CERS5, CERS6, DEGS1, and GBA in PD. **e** Violin plots show module scores for ceramide biosynthesis genes across 22 transcriptionally defined cell types identified in bulk RNA-seq dataset GSE156776. comparing Con (gray) and IPD (yellow) groups. Scores were calculated using Seurat's AddModuleScore with genes involved in ceramide synthesis. Statistical significance was assessed using the Wilcoxon rank-sum test (ns not significant, $^{*}p < 0.05$; $^{**}p < 0.01$; $^{***}p < 0.001$; $^{****}p < 0.0001$). **f** Gene ontology (GO) enrichment analysis of ceramide biosynthesis–associated genes. Bar graph shows significantly enriched GO biological processes related to ceramide metabolism (FDR < 0.05). Data presented as gene count per GO term and adjusted *p*-value.

vehicle-treated A53T mice. However, the extent of p-α-synuclein-positive immunoreactivity was notably reduced following myriocin administration (Fig. 3h and Supplementary Fig. 3).

Transcriptomic analysis reveals normalization of pathological gene expression profiles in A53T mice following myriocin administration

Transcriptomic analysis was performed on three brain regions (cortex, hippocampus, and midbrain) isolated from wild-type, vehicle-treated A53T, and myriocin-treated A53T mice. A comparative evaluation of DEGs revealed that the midbrain, which represents the primary region affected by dopaminergic neuronal loss[22], exhibited the most significant transcriptional alterations and the highest number of DEGs that were statistically significant in both experimental comparisons (vehicle-treated A53T vs. wild-type and myriocin-treated A53T vs. vehicle-treated A53T) (Fig. 4a).

DEGs in midbrain transcriptomes were visualized via a volcano plot (Fig. 4b), showcasing distinct transcriptional profiles between vehicle-administered A53T mutant mice and WT controls (left panel) as well as between myriocin-treated and vehicle-treated A53T transgenic animals (right panel). Vehicle-treated A53T mice exhibited significant upregulation of multiple inflammatory mediators, including C-C motif chemokine ligand 21a (*Ccl21b*) and *Ccl21a*[23]. Following pharmacological inhibition of ceramide synthesis through the administration of myriocin, a marked reversal of these pathological transcriptional changes was observed. Genes associated with neuronal function and synaptic transmission, such as G-protein subunit gamma (*Gng8*)[24] and calmin (*Clmn*)[25], showed significant upregulation after myriocin treatment. Conversely, the expression of several inflammation-related genes, including complement c1qb (*C1qb*)[26] and exocyst complex component 3-like 2 (*Exoc3l2*)[27] was significantly reduced. These transcriptional changes indicate that myriocin effectively mitigates inflammatory responses while simultaneously promoting genes associated with neuronal health and synaptic function (Fig. 4b). Pathway analysis revealed that immune response-related genes were significantly enriched in vehicle-treated A53T mice compared to wild-type controls (Supplementary Fig. 4a, b). Following myriocin administration, significant upregulation was observed in genes associated with synaptic transmission, cognitive processes, and ion channel functionality (Supplementary Fig. 4c, d). These transcriptional alterations correspond with the behavioral improvements documented in myriocin-treated animals.

A rescue-based comparative analysis was conducted to identify differentially expressed genes (DEGs) that exhibited reversal trends in response to myriocin treatment. Specifically, we selected genes that were downregulated in vehicle-treated A53T mice relative to WT and were subsequently upregulated in PD-myr mice (rescue pattern 1), as well as genes that were upregulated in PD-veh mice and reversed in PD-myr mice toward WT levels (rescue pattern 2). Z-score–normalized heatmaps visualized these bidirectional patterns (Fig. 4c, e). Pathway enrichment analysis of rescue pattern 1 genes revealed functional restoration in synaptic signaling, cognition, and neuroplasticity (Fig. 4d), whereas rescue pattern 2 genes were significantly enriched for immune and inflammatory response pathways (Fig. 4f). These findings suggest that myriocin treatment normalizes pathological gene expression programs across distinct molecular pathways. Gene set enrichment analysis (GSEA) confirmed the enhancement of neuronal signaling pathways and the suppression of immune responses following myriocin administration (Supplementary Fig. 4d). GSEA revealed that myriocin administration enhanced neuronal signaling pathways while suppressing immune responses (Supplementary Fig. 4d). Additionally, GSEA revealed significant upregulation of genes involved in mitophagy and mitochondrial homeostasis and marked downregulation of genes associated with inflammation and apoptosis (Fig. 4g). This bidirectional modulation of critical cellular pathways suggests that inhibiting ceramide synthesis may exert neuroprotective effects by promoting mitochondrial quality control and attenuating inflammatory and cell death processes simultaneously. These transcriptomic alterations suggest that inhibiting ceramide synthesis normalizes pathological gene expression patterns, supporting myriocin's potential neuroprotective effects in PD.

Inhibiting ceramide biosynthesis reduces α-synuclein aggregation and enhances mitophagy in patient-derived PD models

To evaluate the therapeutic potential of inhibiting ceramide synthesis in a clinical context, we examined the effects of myriocin in reducing ceramide levels within patient-derived primary neurons. We evaluated mitophagy by transfecting primary neurons derived from patients with PD with the mt-Keima plasmid[28] and subsequently treating them with myriocin. Myriocin significantly increased red fluorescence (561 nm), indicative of increased mitophagic flux (Fig. 5a). Quantitative analysis revealed that concentrations of 10 μM and 50 μM of myriocin increased the Ex561/Ex455 ratio beyond that of vehicle controls, demonstrating elevated mitophagic flux (Fig. 5b). Consistent with these findings, myriocin treatment restored the morphology of the mitochondrial network, as evidenced by improved organization and structure when compared to vehicle-treated neurons (Fig. 5c, d).

To investigate the role of ceramide on α-synuclein aggregation and neurotoxicity within a human PD model, we generated midbrain organoids from induced pluripotent stem cells (iPSCs) obtained from healthy controls and patients with PD (Supplementary Fig. 5a). Vehicle-treated PD organoids exhibited a significant loss of TH-positive neurons and increased accumulation of phosphorylated α-synuclein, indicative of enhanced aggregation and neurotoxicity. Conversely, myriocin treatment significantly restored the viability of TH-positive neurons and decreased levels of phosphorylated α-synuclein, supporting a neuroprotective effect (Fig. 5e and Supplementary Fig. 5b, c). To further assess the impact of ceramide, we supplemented the organoids with ceramides (C16 and C24), which increased phosphorylated α-synuclein aggregation and reduced the area of TH-positive neurons, particularly in PD-derived organoids. These results suggest that ceramide accumulation directly contributes to α-synuclein pathology and that myriocin-mediated inhibition protects dopaminergic neurons (Fig. 5f and Supplementary Fig. 5d, e).

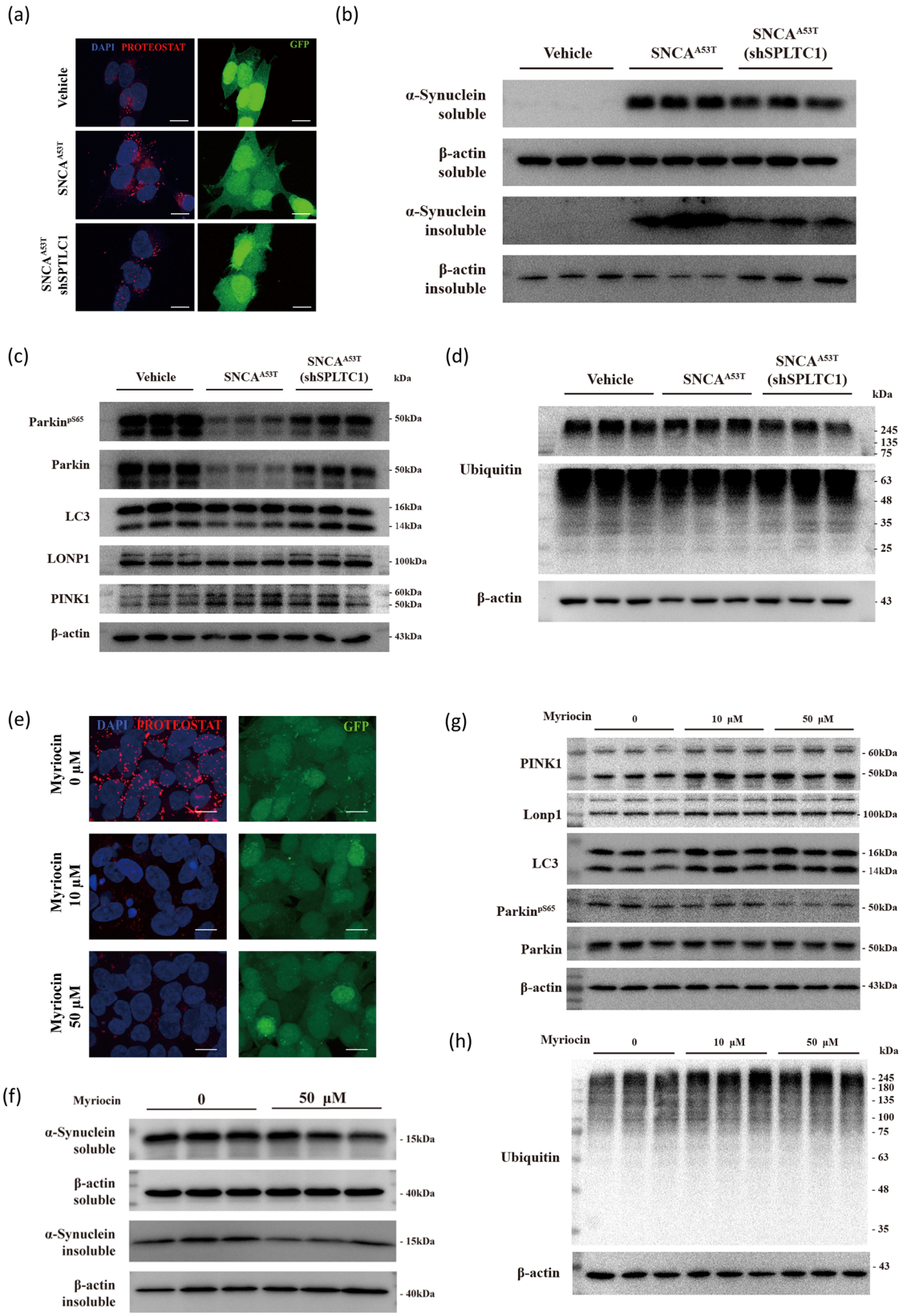

Discussion

In this study, we demonstrate that inhibiting ceramide synthesis reduces α-synuclein accumulation and dopaminergic neuronal degeneration by activating mitophagy in both in vitro and in vivo models. Ceramide concentrations were significantly higher in the brains of patients with LBD compared to controls (Fig. 1a), and snRNA-seq data indicated upregulation of genes involved in ceramide biosynthesis within the midbrain neurons of patients with PD (Fig. 1d, e). These observations are consistent with previous reports demonstrating increased ceramide levels in the blood and cerebrospinal fluid of PD patients relative to healthy controls[29]. In cellular

Fig. 2 | Inhibition of ceramide synthesis alleviates α-synuclein aggregation by enhancing mitophagy in SH-SY5Y neuroblastoma cells. a Representative confocal images of SH-SY5Y cells stably expressing GFP-tagged A53T-mutant α-synuclein (green), with or without genetic silencing of *SPTLC1*. Protein aggregates were detected using ProteoStat dye (red), and nuclei were counterstained with DAPI (blue). Knockdown of *SPTLC1* reduced visible aggregate burden. Scale bars, 10 μm. **b** Immunoblot analysis of Triton X-100–soluble and –insoluble α-synuclein fractions. SH-SY5Y cells overexpressing A53T α-synuclein (A53T-SY5Y) showed decreased accumulation of insoluble α-synuclein following *SPTLC1* knockdown. β-actin served as the loading control. **c** Immunoblot showing mitophagy-related protein changes upon *SPTLC1* knockdown in A53T-SY5Y cells. Increased levels of phospho-parkin (Ser65), LC3-II, and Lonp1 were observed, consistent with enhanced mitophagic flux. **d** Total ubiquitinated protein levels were elevated in A53T-SY5Y cells upon *SPTLC1* knockdown, as assessed by anti-ubiquitin Western blotting, indicating improved proteostatic clearance. **e** Confocal images of A53T-SY5Y cells treated with vehicle or myriocin (10 μM or 50 μM, 48 h). Aggregation was visualized using ProteoStat dye. Myriocin reduced α-synuclein aggregation similar to genetic *SPTLC1* suppression. Scale bars, 10 μm. **f** Western blot of A53T-SY5Y cells treated with 10 or 50 μM myriocin for 48 h. Myriocin increased levels of PINK1, LC3-II, and Lonp1 in a dose-dependent manner, indicating enhanced mitophagy. **g** Immunoblot analysis of total ubiquitinated proteins in myriocin-treated A53T-SY5Y cells. Myriocin treatment elevated ubiquitin levels, reflecting enhanced protein clearance. β-actin was used as a loading control. Uncropped western blot images are provided in Supplementary Fig. 6.

assays, both genetic and pharmacological suppression of SPT led to significant reductions in insoluble α-synuclein levels in SH-SY5Y cells expressing the A53T mutant SNCA, along with increased mitophagy indicators, including parkin phosphorylation and LC3-II levels (Fig. 2c, f). Collectively, these findings implicate ceramide accumulation in neurodegeneration by facilitating α-synuclein aggregation and disrupting mitochondrial quality control processes.

Importantly, our in vivo experiments further validated these effects, showing that myriocin treatment significantly improved both motor performance and spatial memory in A53T mice (Fig. 3d, e). This functional improvement was accompanied by a reduction in phosphorylated α-synuclein levels and preservation of TH-positive dopaminergic neurons (Fig. 3g, h). These results align with previous findings in aged muscle, where ceramide inhibition promoted mitochondrial homeostasis and proteostasis[10]. Transcriptomic analyses of midbrain tissues from myriocin-treated mice revealed normalization of gene expression networks related to synaptic function, mitochondrial dynamics, and immune responses (Fig. 4d, f, g). This suggests that ceramide synthesis inhibition not only reduces protein aggregation but also restores homeostatic signaling pathways critical for neuronal survival.

Our analysis revealed elevated C18-ceramide levels in both human LBD and A53T mouse midbrain. C18-ceramide is produced by CERS1[30], the predominant ceramide synthase in neurons. Notably, SPTLC1 expression was modestly reduced in human PD neurons, potentially reflecting compensatory downregulation in response to chronic ceramide accumulation. However, the ceramide biosynthesis module score remained elevated across multiple cell types, indicating sustained pathway activation despite this single-gene change. Myriocin treatment reduced C18-ceramide levels and normalized ceramide pathway gene expression, demonstrating that SPT inhibition can reverse this metabolic dysfunction and its associated neurotoxicity.

The relevance of our findings was further supported by experiments using primary neurons and human midbrain organoids derived from PD patient iPSCs (Fig. 5). Myriocin treatment significantly decreased α-synuclein aggregation and preserved dopaminergic neuron populations, thereby reinforcing the translational potential of targeting ceramide metabolism (Fig. 5d). Additionally, the detrimental effects observed from exogenous ceramide supplementation on α-synuclein aggregation and dopaminergic neuron survival in organoids highlight the pathological role of ceramide accumulation (Fig. 5e). Interestingly, ceramide supplementation in normal midbrain organoids similarly increased the area of TH-positive neurons (Supplementary Fig. 4d), suggesting that ceramide may play a role in neuronal development and maintenance. However, excessive accumulation of ceramide appears detrimental, leading to neuronal damage and dysfunction. This dual role indicates that ceramide levels must be carefully regulated: physiological concentrations may support neuronal integrity, while pathological accumulation contributes to neurodegeneration[30,31].

Our study has several limitations. First, although we demonstrated that myriocin effectively reduces ceramide levels and ameliorates α-synuclein pathology, the long-term safety profile associated with chronic ceramide synthesis inhibition remains to be established[32]. Myriocin reduced several pathologically relevant ceramide species in the brains of PD mice. However, some subspecies showed modest increases, possibly due to compensatory activation of the salvage pathway[33]. Further studies should include detailed lipidomic time courses to better understand ceramide dynamics under SPT inhibition. Second, while our findings highlight the beneficial effects of ceramide synthesis inhibition on α-synuclein pathology, PD pathophysiology is complex and involves various contributing factors, such as genetic predispositions and environmental influences[34]. Third, while our data reveal associations between α-synuclein pathology and altered ceramide metabolism at transcriptomic and lipidomic levels, the direct mechanisms by which α-synuclein influences ceramide biosynthesis and how ceramide accumulation promotes α-synuclein aggregation remain unclear. Further studies are needed to clarify these molecular interactions. Fourth, although midbrain organoids provide valuable insights into human disease processes, they lack the complexity of neural circuitry and systemic influences that may modulate treatment responses in patients. Additionally, we did not directly quantify ceramide levels in A53T-SY5Y cells, primary neurons, or midbrain organoids. Therefore, while myriocin treatment resulted in functional improvements, the lack of lipidomic data in these models limits our ability to quantitatively correlate these effects with specific reductions in ceramide species. Future studies should include targeted lipidomic profiling to verify ceramide modulation and establish the mechanistic relationship between ceramide dysregulation and α-synuclein pathology in these in vitro models.

In conclusion, our results suggest that targeting ceramide synthesis represents a novel and promising therapeutic approach for PD. By reducing protein aggregation and enhancing mitophagic flux, myriocin treatment addresses key pathogenic mechanisms prevalent in α-synuclein-related neurodegeneration. Further studies are warranted to explore the clinical applicability of ceramide inhibition in PD and related neurodegenerative disorders characterized by protein aggregation.

Methods

Study design

This study was designed to evaluate whether the inhibition of de novo ceramide synthesis by myriocin confers neuroprotective effects in models of Parkinson's disease (PD) through modulation of α-synuclein aggregation and mitophagy. A multi-tiered experimental strategy was employed, encompassing transcriptomic analysis of human postmortem midbrain tissue, in vitro validation utilizing α-synuclein-overexpressing neuronal cells, and in vivo efficacy testing in a transgenic A53T α-synuclein mouse model. The therapeutic relevance was further evaluated using patient-derived dopaminergic neurons and midbrain organoids. For in vitro cell line experiments, three to four biological replicates per condition were tested, with each experiment repeated independently at least three times to ensure reproducibility.

Myriocin treatment was initiated in A53T mice during the symptomatic phase, and effects were evaluated via behavioral, biochemical, and histological endpoints. The number of animals per group was

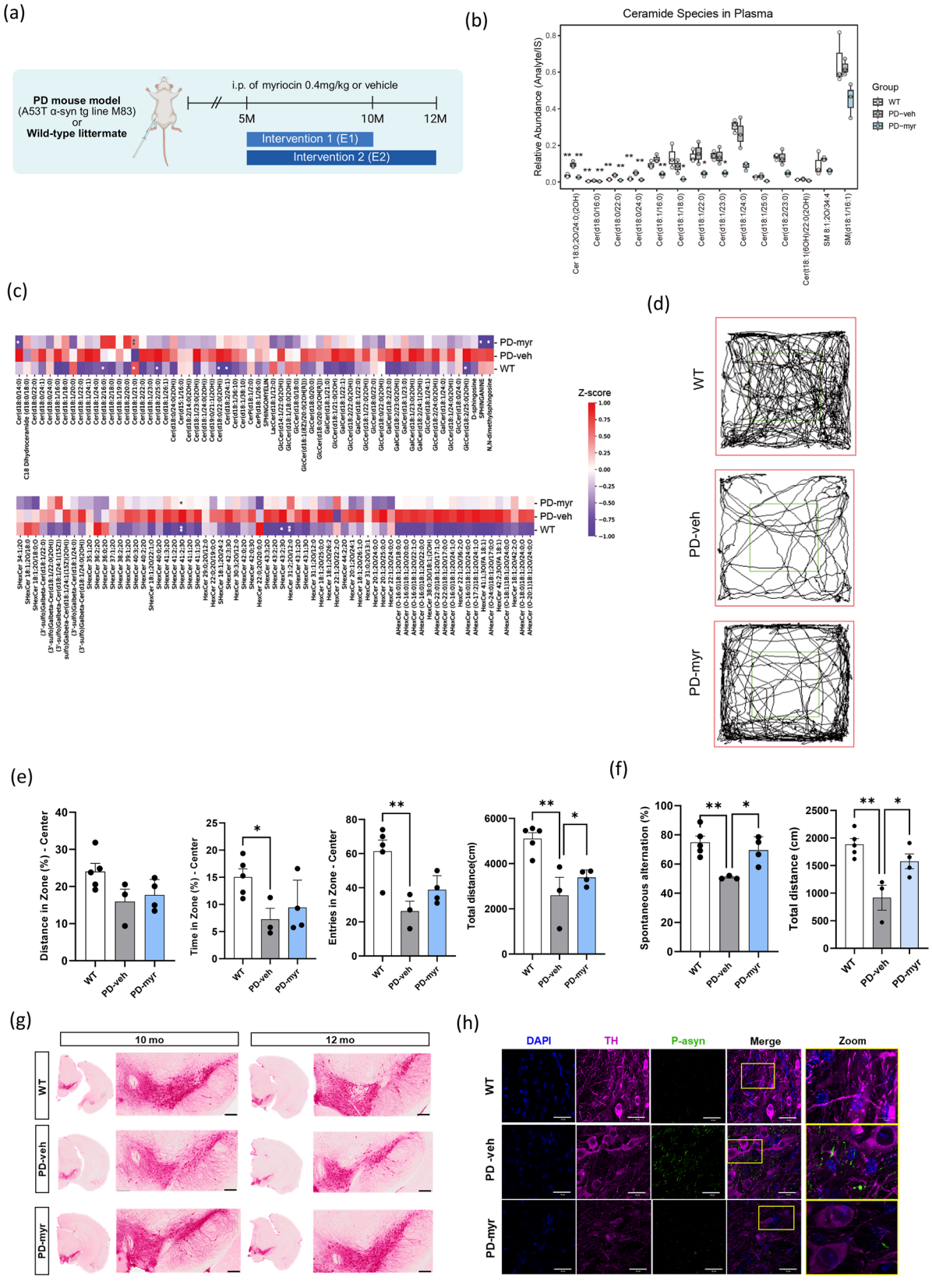

determined to ensure reproducibility while minimizing usage, in accordance with institutional animal care guidelines. Five to six female mice were used per group across all treatment conditions. Mice were grouped based on age to maintain homogeneity across experimental cohorts. Behavioral and histological evaluations were conducted by investigators blinded to treatment conditions. Blinding was also applied to cell and organoid experiments to mitigate bias. This comprehensive approach facilitated an extensive evaluation of myriocin as a potential disease-modifying therapy across both human-derived and animal-based PD models.

Fig. 3 | Myriocin treatment attenuates α-synuclein pathology, ceramide accumulation, and behavioral deficits in A53T α-synuclein transgenic mice. **a** Schematic overview of the treatment regimen in A53T α-synuclein transgenic mice (M83 line). Myriocin (0.4 mg/kg, i.p.) or vehicle was administered three times per week starting at 5 months of age for either 5 months (E1) or 7 months (E2). Relative levels of ceramide species in (**b**) plasma and (**c**) midbrain tissue measured by ultra-high-performance liquid chromatography–mass spectrometry (UHPLC-MS). **b** Quantification of ceramide species in plasma of wild-type (WT), vehicle-treated PD (PD-veh), and myriocin-treated PD (PD-myr) mice. Several long-chain ceramide species were significantly elevated in PD-veh mice and reduced by myriocin treatment. **c** Heatmap showing relative abundance of individual ceramide species in the midbrain of WT, PD-veh, and PD-myr mice. Ceramide levels were normalized to total lipid content. Myriocin reduced multiple ceramide species elevated in PD-veh mice. Asterisks indicate statistical significance compared with the PD-veh group (one-way ANOVA followed by Dunnett's post hoc test). $^{*}p < 0.05$, $^{**}p < 0.01$, $n = 3$ per group. **d** Representative locomotor traces from the open field test showing reduced center exploration and hypoactivity in PD-veh mice, partially restored by myriocin. **e** Behavioral quantification from open field testing. PD-veh mice exhibited reduced distance, time, and entries in the central zone as well as decreased total distance traveled, all significantly improved by myriocin treatment ($n = 3$–5 mice per group). **f** Y-maze spontaneous alternation test. PD-veh mice showed impaired spatial working memory, as indicated by lower alternation percentage, significantly improved in the PD-myr group ($n = 3$–5 mice per group). **g** Tyrosine hydroxylase (TH) immunohistochemistry of midbrain sections from PD-veh and PD-myr mice at 10 and 12 months of age. Myriocin preserved TH-positive neurons in the substantia nigra pars compacta and ventral tegmental area. Scale bars, 200 μm. **h** Immunofluorescence images showing DAPI (blue), TH (magenta), and phospho–α-synuclein (pS129, green) in the substantia nigra. Myriocin treatment reduced pathological pS129 α-synuclein immunoreactivity. Insets show magnified views of boxed regions. Scale bars, 30 μm. $^{*}p < 0.05$; $^{**}p < 0.01$.

Sample preparation for ceramide analysis

Postmortem midbrain tissues from individuals diagnosed with Lewy body dementia (LBD; $n = 6$) and age-matched neurologically healthy controls ($n = 6$) were obtained from the Korea Brain Bank with institutional review board (IRB) approval (Supplementary Table 1). Tissue sections were dissected from the substantia nigra pars compacta (SNpc) and immediately snap-frozen. Although the ventral tegmental area (VTA) is anatomically part of the midbrain, it shows relative preservation in PD pathology[35,36] and was not included in our sampling. This study only analysed SNpc tissue to focus on the region most relevant to PD pathology. Brain tissue samples were processed for ultra-performance liquid chromatography-Orbitrap mass spectrometry (UPLC-Orbitrap-MS) analysis, following adjusted protocols based on methods described by Lee et al.[37]. Briefly, 10 mg of frozen tissue was homogenized in 100 μL of ice-cold phosphate-buffered saline (PBS). A 30 μL aliquot of the homogenate was transferred to a new tube and spiked with 2 μL of internal standard (Deuterated Ceramide LIPIDOMIX™ Mass Spec Standard, Avanti Research™, USA). The internal standard mixture consisted of C16 Ceramide-d7 (d18:1-d7/16:0), C18 Ceramide-d7 (d18:1-d7/18:0), C24 Ceramide-d7 (d18:1-d7/24:0), and C24:1 Ceramide-d7 (d18:1-d7/24:1). For lipid extraction, 600 μL of ice-cold methanol containing 1 mM butylated hydroxytoluene (BHT) and chloroform (1:2, v/v) was added to each sample. The mixture was vortexed, followed by 10 s of sonication, and then incubated on ice for 30 min. To induce phase separation, 150 μL of distilled water was incorporated, and the samples were centrifuged at 14,000 rpm for 5 min at 4 °C. A volume of 250 μL was collected from the lower organic layer. The remaining aqueous phase underwent a secondary extraction using the previously described protocol, and the resulting organic layer (350 μL) was combined with the initial extract. The pooled organic phase was dried in a vacuum concentrator and was reconstituted in 100 μL of the same solvent as mobile phase B (0.1% formic acid and 2 mM ammonium formate in isopropanol:acetonitrile = 9:1, v/v) for subsequent liquid chromatography-mass spectrometry (LC-MS) analysis.

UPLC-Orbitrap-MS based ceramide profiling

Ceramide profiling was performed using a Vanquish Flex ultra-high-performance liquid chromatography (UHPLC) system coupled with an Orbitrap Exploris 120 mass spectrometer (Thermo Fisher Scientific, San Jose, CA, USA) at the Biopolymer Research Center for Advanced Materials, Sejong University (Seoul, Republic of Korea). Chromatographic separation was achieved using an ACQUITY UPLC BEH C18 column (2.1 × 100 mm, 1.7 μm, Waters, USA) with the column temperature maintained at 45 °C. The mobile phase system consisted of solvent A (60% acetonitrile with 2 mM ammonium formate and 0.1% formic acid) and solvent B (isopropanol:acetonitrile, 90:10, v/v, containing the same additives). The gradient elution was programmed as follows: starting at 10% B (0–1 min), increasing to 70% B (1–6 min), then to 90% B (6–12 min), followed by a step to 100% B (12–13 min), and returning to 10% B for column re-equilibration (13–16 min). The flow rate was maintained at 0.4 mL/min. Data acquisition was performed in both positive and negative ionization modes using full MS scans combined with data-dependent tandem mass spectrometry (MS/MS) acquisition. Instrument parameters included a spray voltage of 4.0 kV, capillary temperature of 325 °C, heater temperature of 40 °C, and sheath/auxiliary gas flows of 50 and 10 arbitrary units, respectively. The S-lens radiofrequency (RF) level was set to 70%. Sample injection order was randomized to minimize run-order effects. Quality control (QC) samples, prepared by pooling aliquots from all study samples, were injected every 10 runs to monitor analytical reproducibility and stability. Full scan and data-dependent MS/MS spectra were acquired using Xcalibur 4.6, and raw data were pre-processed using Compound Discoverer 3.3 (Thermo Fisher Scientific). Ceramide species were identified based on characteristic MS/MS fragment patterns. Differential levels of ceramides between experimental groups were assessed using Student's *t*-test. A *p*-value of less than 0.05 was considered statistically significant.

Human brain tissue transcriptomic analysis

Single-nucleus RNA-sequencing (snRNA-seq) data were reanalyzed from the publicly available dataset GSE243639. Data were processed using the Seurat package (v4.3.0) with standard quality control procedures, normalization (SCTransform), dimensionality reduction, and clustering. Cell types were annotated based on canonical marker expression. Differentially expressed genes (DEGs) were assessed using the Wilcoxon rank-sum test and corrected for multiple testing using the Benjamini-Hochberg method. Gene set enrichment analysis (GSEA) was performed using the clusterProfiler package with curated gene sets relevant to ceramide metabolism, mitophagy, and α-synuclein biology. Additionally, bulk RNA sequencing data from GSE156776 were used to validate cell–type–specific alterations in the expression of ceramide biosynthesis-related genes.

To evaluate ceramide biosynthesis activity at the single-cell level, we calculated a module score using the AddModuleScore function in Seurat (v5.2.1). The gene set was curated from published literature on enzymes of de novo ceramide synthesis[38–42]. It included initiation (SPTLC1, SPTLC2, SPTSSA, SPTSSB)[39], reduction (KDSR)[42], N-acylation (CERS1–6)[42], desaturation (DEGS1, DEGS2)[41], and hydroxylation (FA2H)[38]. The score was calculated by averaging the expression of these genes in each cell and adjusting against matched control gene sets. The ceramide biosynthesis score, based on literature-curated genes, reflects pathway activity at the single-cell level, although the pathway is not yet completely defined. Scores were compared between control and idiopathic Parkinson's disease (IPD) groups across different cell types using the Wilcoxon rank-sum test.

SH-SY5Y cell culture and genetic/pharmacologic manipulation

SH-SY5Y human neuroblastoma cells (ATCC CRL-2266) were maintained in DMEM/F-12 (Gibco) supplemented with 10% fetal bovine serum (FBS; Gibco) and 1% penicillin-streptomycin at 37 °C in a 5% CO_2 incubator. Cells were passaged every 2–3 days using 0.05% Trypsin-EDTA. To model α-synuclein pathology, cells were electroporated with plasmids carrying the

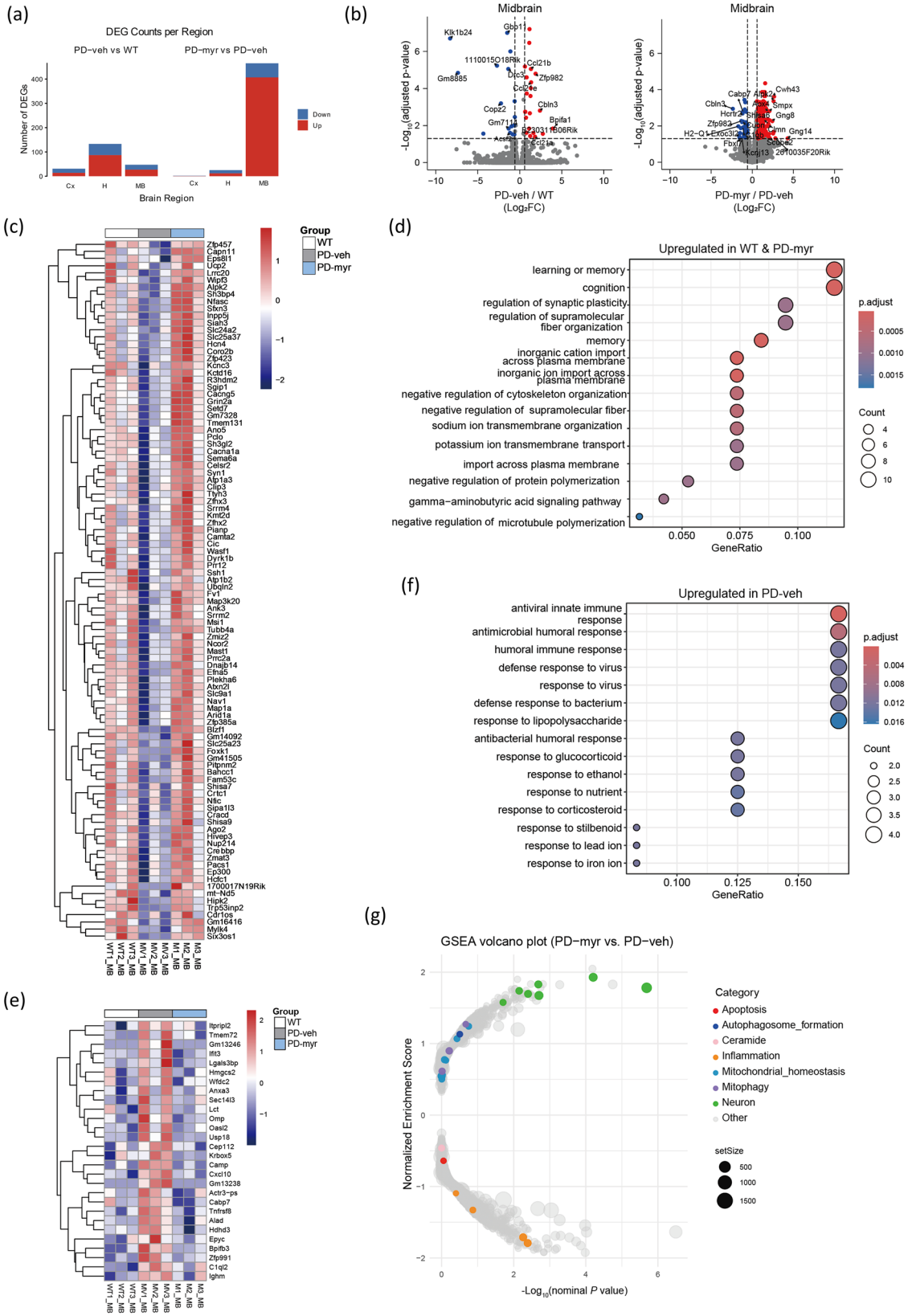

human A53T-mutant α-synuclein ($SNCA^{A53T}$) using the Neon Transfection System (Thermo Fisher Scientific). Electroporation was performed using 5×10^5 cells per 10 µL, 1 µg DNA, under the following settings: 1200 V, 20 ms, and 3 pulses. In select experiments, the knockdown of serine palmitoyltransferase long chain base subunit 1 (SPTLC1) was achieved by co-electroporation with the shSPTLC1 plasmid (pLKO.1-U6-puro-shSPTLC1).

Pharmacologic inhibition of ceramide synthesis was achieved by treating cells with 10 or 50 µM myriocin (Sigma-Aldrich, M1177) for 48 h, consistent with concentrations shown to reduce ceramide levels in neuronal

Fig. 4 | Myriocin reverses transcriptomic signatures of neuroinflammation and synaptic dysfunction in the midbrain of A53T α-synuclein transgenic mice. a Bar plot showing the number of differentially expressed genes (DEGs; adjusted $p < 0.05$, $|\log_2FC| > 0.58$) across three brain regions (cortex, hippocampus, and midbrain) in pairwise comparisons: PD-veh vs. WT and PD-myr vs. PD-veh. The midbrain displayed the highest number of DEGs in response to myriocin treatment (PD-myr vs. PD-veh), indicating a region-specific transcriptional effect. **b** Volcano plots illustrating midbrain DEGs in PD-veh vs. WT (left) and PD-myr vs. PD-veh (right) comparisons. Red dots indicate upregulated genes and blue dots indicate downregulated genes (adjusted $p < 0.05$, $|\log_2FC| > 0.58$). Myriocin treatment reversed many inflammation-related gene changes observed in PD-veh mice. **c** Heatmap showing Z-score–normalized expression of genes downregulated in PD-veh mice but upregulated in both WT and PD-myr groups (rescue pattern 1). **d** Gene Ontology (GO) enrichment analysis of rescue-pattern genes in panel (**c**), indicating restored pathways related to synaptic transmission, learning, and cognition. **e** Heatmap showing Z-score–normalized expression of genes upregulated in PD-veh but decreased in WT and PD-myr groups (rescue pattern 2), many of which are associated with immune or inflammatory responses. **f** GO enrichment analysis of genes in (**e**), highlighting biological processes such as interferon signaling and innate immune response that were reversed by myriocin. **g** Gene Set Enrichment Analysis (GSEA) volcano plot showing gene sets significantly modulated by myriocin (PD-myr vs. PD-veh). Myriocin increased the expression of gene sets related to mitophagy, mitochondrial homeostasis, and neuronal signaling, while downregulating pathways associated with inflammation, apoptosis, and ceramide metabolism. All downstream transcriptomic analyses were performed on midbrain tissues ($n = 3$ mice per group). DEGs were identified using DESeq2 with Benjamini–Hochberg FDR correction.

cell lines[8]. Vehicle controls were treated with 0.1% DMSO. Protein aggregation was assessed using the ProteoStat Aggresome Detection Kit (Enzo Life Sciences, ENZ-51035-0025). Following fixation with 4% paraformaldehyde and permeabilization with 0.1% Triton X-100, cells were stained with ProteoStat dye and counterstained with DAPI. Aggregates were visualized using a confocal microscope (FV3000RS, Olympus, Tokyo, Japan).

For detergent-based fractionation of α-synuclein, cells were lysed in PBS containing 1% Triton X-100 with protease and phosphatase inhibitors, and centrifuged at 21,000 *g* for 15 min at 4 °C. The supernatant was collected as the Triton-soluble fraction. The remaining pellet was washed twice and lysed in 7 M urea/RIPA buffer containing 1% sodium dodecyl sulfate (SDS), 100 U/mL Benzonase, and protease/phosphatase inhibitors. After incubation at room temperature for 20 min, samples underwent five freeze–thaw cycles (1 min liquid nitrogen, 1 min 37 °C water bath) and were centrifuged at 21,000 *g* for 20 min at 4 °C. The supernatant was collected as the Triton-insoluble fraction[43].

Western blotting was performed using both fractions. Proteins were quantified with the DC Protein Assay (Bio-Rad), separated by 8–14% SDS-PAGE, and transferred to polyvinylidene fluoride (PVDF) membranes. Membranes were blocked with 5% skim milk for 1 h and incubated overnight at 4 °C with primary antibodies against α-synuclein (BD, 610786), p-α-synuclein (Abcam ab184674), PINK1 (CST, 6946), Parkin (CST, 32833), p-Parkin (CST, 36866), LC3A/B (CST, 4108), Lonp1 (NOVUS, H00010561-D01P), Ubiquitin (CST, 58395), and β-actin (Abbkine, ABL1010). After washing, membranes were incubated with HRP-conjugated secondary antibodies (CST, 7074 or 7076) for 1 h. Bands were visualized using Clarity ECL (Bio-Rad) and LuminoGraph II (ATTO). Membranes were pretreated with 0.4% paraformaldehyde in PBS for 30 min before blocking to enhance α-synuclein detection[44].

A53T α-synuclein transgenic mouse model and myriocin administration

Mice were bred in a specific pathogen-free environment, adhering to the Gwangju Institute Science and Technology (GIST) Laboratory Animal Resource Center (LARC) guidelines. All experimental procedures involving animals were approved by the Institutional Animal Care and Use Committee (Approval number: GIST-2024–066) at GIST LARC. In this study, female homozygous A53T α-synuclein transgenic mice (line M83; JAX #004479)[21] and age- and sex-matched C57BL/6 J wild-type littermates were used for all in vivo experiments. Mice were randomly assigned to one of two intervention paradigms. In Intervention 1 (E1), myriocin (0.4 mg/kg in phosphate-buffered saline containing 0.3% DMSO) or vehicle was administered intraperitoneally (i.p.) three times per week beginning at 5 months of age and continuing for 5 months based on previous studies demonstrating effective ceramide reduction at this dose in mouse models[10,45]. In Intervention 2 (E2), the same dosing regimen was applied over a 7-month period starting at 5 months of age (Fig. 3a). The myriocin dosage was based on previous studies demonstrating efficacy in sphingolipid inhibition in vivo[45]. Mice were housed in a 12-h light/dark cycle with free access to water and food. Mice were sacrificed at 10 months (E1) or 12 months (E2), followed by sample collection for downstream analyses.

Behavioral tests

Handling and habituation: Mice were handled and habituated to the testing room and experimenter for 2 consecutive days (10 min, 3 sessions) prior to the day of testing for all tests. All behavioral tests were conducted during the light phase by blinded experimenters.

Open field test (OFT): To assess anxiety-like behaviors and locomotor activity, mice were individually placed in the center of a 40 × 40 cm square open-field arena (wall height: 40 cm) for 10 min. The arena was divided into a central zone (20 × 20 cm) and a peripheral zone. Locomotion parameters —including total distance traveled, number of entries into the center zone, time spent in the center zone, and distance traveled within the center—were recorded using a Smart 3 video tracking system (Panlab, Harvard University, USA). The arena was disinfected with 70% ethanol between trials.

Y-maze spontaneous alternation test: Spatial working memory was assessed using a Y-maze apparatus comprising three identical arms (40 cm length × 3 cm width × 12 cm wall height) arranged at 120° angles. Mice were placed at the end of one arm (start arm) and allowed to explore freely for 5 min. Arm entries and spontaneous alternations were recorded via the Smart 3 system. An alternation was defined as sequential entries into three different arms. The spontaneous alternation percentage was calculated as:

$$[(number\ of\ alternations)/(total\ number\ of\ arm\ entries - 2)] \times 100.$$

Between trials, the Y-maze arms were disinfected with 70% ethanol to eliminate odors and residues.

Tissue collection and processing

At the study endpoint, mice were deeply anesthetized with isoflurane delivered via inhalation (3–4% for induction, 1.5–2% for maintenance) using a calibrated vaporizer. Anesthetic depth was confirmed by the absence of pedal and corneal reflexes. While fully unconscious, animals were euthanized by transcardial perfusion with ice-cold PBS. Whole blood was collected from the inferior vena cava during perfusion. Blood samples were centrifuged at 2000 *g* for 10 min at 4 °C to isolate plasma, which was stored at −80 °C for lipidomic analysis. Brains were rapidly harvested on ice, with one hemibrain fixed in 4% paraformaldehyde (PFA; Sigma-Aldrich) overnight at 4 °C, cryoprotected in 30% sucrose, and stored at 4 °C for histological analysis. The contralateral hemibrain was dissected into the olfactory bulb, cortex, hippocampus, midbrain, brainstem, cerebellum, and deep brain structures. Each region was immediately snap-frozen in liquid nitrogen and stored at −80 °C for subsequent lipidomic and transcriptomic analyses.

Immunohistochemistry and immunofluorescence staining

Free-floating coronal cryosections (40 μm) containing the substantia nigra were utilized for histological analyses. Sections were washed in PBS containing 1% Tween-20 (PBS-T) and incubated with BLOXALL® Endogenous

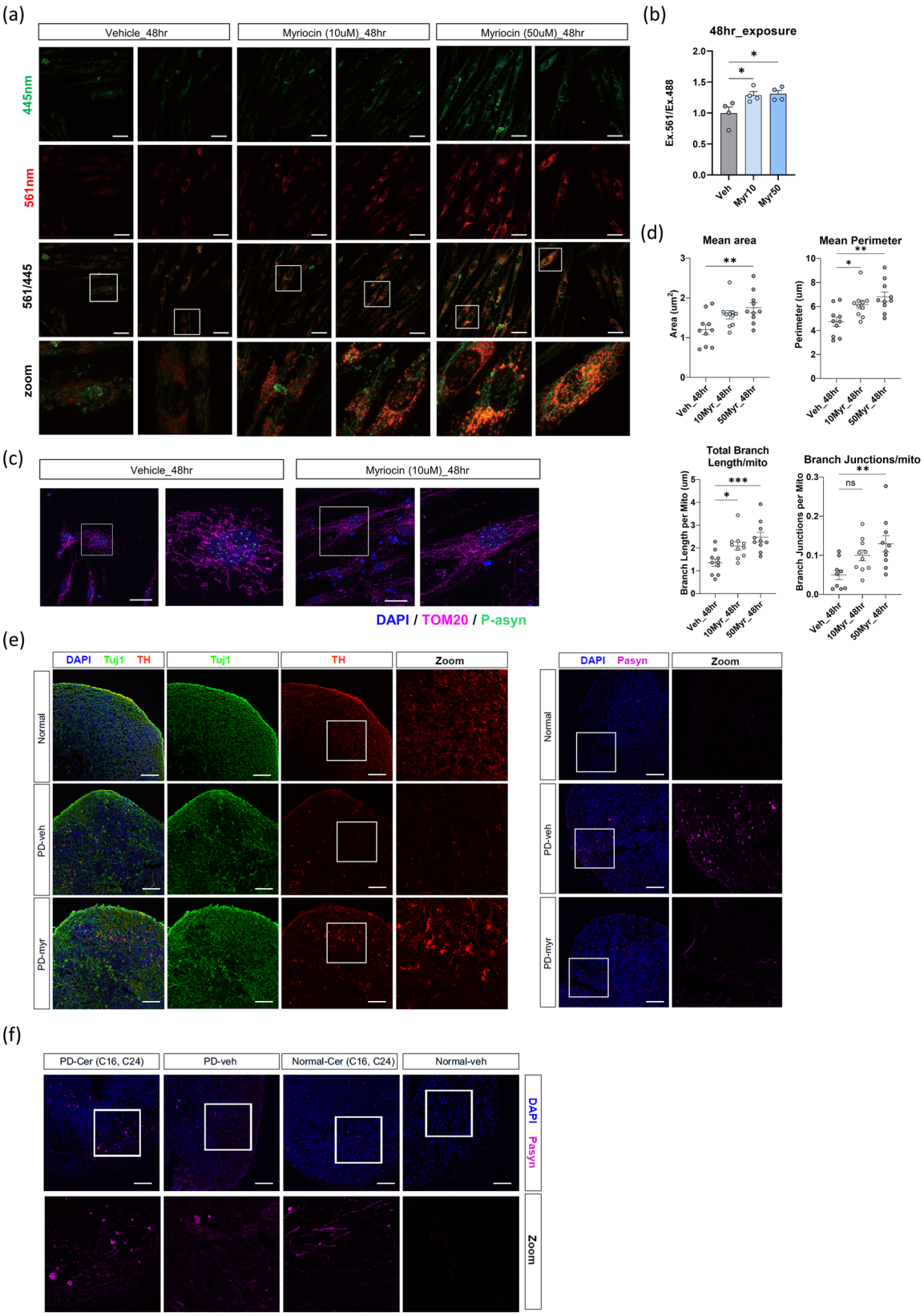

Blocking Solution (Vector Laboratories, SP-6000) for 20 min to quench endogenous peroxidase activity. After washing, sections were blocked with 2% normal serum in PBS-T for 2 h at room temperature, followed by overnight incubation at 4 °C with primary antibody against tyrosine hydroxylase (TH; Novus, OPA1-04050, 1:1000). The next day, sections were washed in PBS-T and incubated with a biotinylated anti-rabbit secondary antibody included in the Alkaline Phosphatase Standard Kit (Vector Laboratories, AK-5200) for 30 min, followed by alkaline phosphatase reagent (Vector Laboratories, AK-5200) for an additional 30 min. Signal was developed using Vector® Red Substrate Kit (Vector Laboratories, SK-

Fig. 5 | Inhibition of ceramide biosynthesis enhances mitophagy and reduces α-synuclein pathology in patient-derived Parkinson's disease models. **a** Representative confocal images of mt-Keima–expressing patient-derived dopaminergic neurons following 48-h treatment with vehicle, 10 μM, or 50 μM myriocin. Cells were imaged at excitation wavelengths of 488 nm (neutral mitochondria, green) and 561 nm (acidified mitolysosomes, red). Merged and zoomed images (bottom) highlight increased red puncta upon myriocin treatment, indicating enhanced mitophagic flux. Scale bars, 50 μm. **b** Quantification of mitophagy levels expressed as the 561/488 nm excitation ratio. Data are presented as mean ± SEM from four independent experiments. $^{*}P < 0.05$ by one-way ANOVA followed by Dunnett's post hoc test for multiple comparisons. **c** Confocal immunofluorescence images of patient-derived neurons treated with vehicle or 10 μM myriocin for 48 h, stained for TOM20 (magenta), phospho-α-synuclein (pS129; green), and DAPI (blue). Myriocin restored mitochondrial network integrity. Scale bars, 50 μm. **d** Quantification of mitochondrial morphology in patient-derived neurons treated with vehicle or myriocin (10 μM or 50 μM) for 48 h. Morphological parameters, including mitochondrial area, perimeter, total branch length, and branch junctions per mitochondrion, were measured using Mitochondria Analyzer in ImageJ. Data represents SEM from $n = 10$ cells per condition. $^{*}p < 0.05$, $^{**}p < 0.01$, $^{***}p < 0.001$ by one-way ANOVA followed by Dunnett's post hoc test for multiple comparisons. **e** Immunofluorescence analysis of midbrain organoid sections from healthy controls, vehicle-treated PD lines, and myriocin-treated PD lines. Left: Co-staining for neuronal markers Tuj1 (green) and tyrosine hydroxylase (TH; red) revealed myriocin-mediated rescue of dopaminergic neuronal loss. Right: Immunostaining for phospho-α-synuclein (pS129; magenta) showed reduced aggregate levels in myriocin-treated organoids. Nuclei were stained with DAPI (blue). Scale bars, 100 μm. **f** Effects of exogenous ceramide supplementation on α-synuclein aggregation in midbrain organoids. Organoids derived from PD or healthy iPSC lines were treated with 10 μM of C16 and C24:1 ceramide mixture for 48 h and stained for pS129 (magenta) and DAPI (blue). Ceramide supplementation increased α-synuclein aggregation in PD-derived organoids. Scale bars, 100 μm.

5100). Sections were mounted, air-dried, and cover-slipped using Aqueous Mounting Medium (Dako, S3025).

For immunofluorescence staining, adjacent SN sections were co-stained for TH, phosphorylated α-synuclein (pS129), and nuclei. Sections were incubated overnight at 4 °C with the same TH antibody (OPA1-04050, 1:1000) and anti–phospho-α-synuclein (Abcam, ab184674, 1:1000), diluted in PBS-T with 2% normal serum. Following PBS washes, sections were incubated with Alexa Fluor 647–conjugated donkey anti-rabbit IgG (Abcam, ab150075, 1:1000) and PE-conjugated anti-mouse IgG $F(ab')_2$ (Cell Signaling Technology, #8887S, 1:1000) for 1 h at room temperature. DAPI (Thermo Fisher, D1306, 1 μg/mL) was used for nuclear counterstaining. Whole-slide images of immunostained sections were acquired using a high-resolution slide scanner (VS200, Olympus, Tokyo, Japan) operated with OlyVIA software (version 3.3). Z-stack images were collected using 20× brightfield mode, and representative sections were selected for downstream visualization. All scanning parameters, including exposure and gain, were kept constant across samples to ensure comparability.

Mouse bulk RNA-seq preparation and analysis

Total RNA was isolated from frozen cortex, hippocampus, and midbrain tissues using TRIzol reagent (Thermo Fisher Scientific), according to the manufacturer's protocol. RNA quality was assessed with the Quant-iT RiboGreen RNA Assay Kit (Invitrogen, #R11490) and Agilent TapeStation using RNA ScreenTape (#5067-5576). Only samples with an RNA Integrity Number (RIN) > 7.0 were utilized for library preparation. RNA libraries were prepared using the TruSeq Stranded Total RNA Library Prep Gold Kit (Illumina, #20020599), which includes ribosomal RNA depletion. mRNA fragmentation was performed under elevated temperatures in the presence of divalent cations. First-strand cDNA was synthesized using SuperScript II Reverse Transcriptase (Invitrogen, #18064014) with random primers, followed by second-strand synthesis incorporating dUTP. After end repair, A-tailing, and adapter ligation, libraries were PCR-amplified, quantified using the KAPA Library Quantification Kit (Roche, #KK4854), and quality-checked with Agilent D1000 ScreenTape (#5067-5582). Paired-end sequencing (2 × 150 bp) was performed on an Illumina NovaSeq X platform (Macrogen Inc., Seoul, South Korea). Raw reads were aligned to the mouse reference genome (mm10) and quantified at the gene level using FeatureCounts. Gene counts were processed in R (v4.3.0) using the DESeq2 package (v1.38.0). Genes with counts per million (CPM) > 0.5 in at least two samples were retained (~21,800 genes). Samples were grouped by brain region and experimental condition. Variance stabilizing transformation (VST) was applied for visualization. Principal component analysis (PCA) was used to assess sample clustering. Differential expression analysis was conducted using DESeq2 for each brain region, with contrasts defined as PD-myr vs. PD-veh and PD-veh vs. WT. Genes with absolute $\log_2$ fold change > 0.58 and adjusted $p < 0.05$ were considered differentially expressed. Gene annotation was performed using the org.Mm.eg.db and AnnotationDbi packages. Differentially expressed genes were analyzed for Gene Ontology (GO) and Kyoto Encyclopedia of Genes and Genomes (KEGG) pathway enrichment using clusterProfiler. Data visualization included volcano plots (EnhancedVolcano), heatmaps (pheatmap), and dot plots (ggplot2). Gene Set Enrichment Analysis (GSEA) was performed using the gseGO function in the clusterProfiler package, based on gene rankings reflecting transcriptional rescue effects, calculated as the average expression in WT and PD-myr conditions relative to PD-veh. Zscore–normalized heatmaps were used to visualize condition-specific and reversed expression patterns.

Patient-derived neuron culture and mitophagy imaging

Human iPSC-derived neural progenitor cells (NPCs) derived from a Parkinson's disease patient (ATCC, ACS-5001) were expanded in DMEM/F-12 (ATCC, 30-2006) supplemented with NPC Growth Kit components (ATCC, ACS-3003), following the manufacturer's instructions. For differentiation, NPCs were plated on Cell Basement Membrane Gel–coated 12-well plates and cultured in Dopaminergic Neuron Differentiation Medium (ATCC, ACS-3004) with medium changes every 2–3 days. Neuronal differentiation was performed for 3 weeks prior to experimentation. NPCs underwent electroporation with a mitochondrially targeted Keima plasmid (mtKeima; provided by Dr. Dong-Ryeol Ryu) using the Neon Transfection System (Thermo Fisher Scientific) in accordance with the manufacturer's protocol (1×10^6 cells in 10 μL buffer with 5 μg plasmid DNA). After electroporation, cells were plated and maintained in NPC growth medium containing puromycin for 3 weeks to allow stable mt-Keima expression prior to neuronal differentiation. Myriocin (10 or 50 μM) or vehicle (0.1% DMSO) was applied for 48 h to mt-Keima–expressing dopaminergic neurons. Following pre-treatment, cells were either fixed or subjected to live-cell imaging. Live-cell mitophagy imaging was performed using a confocal microscope (FV3000RS, Olympus, Tokyo, Japan) equipped with 445 nm and 561 nm lasers. Neutral mitochondria were excited at 445 nm and mitolysosomes at 561 nm, with emission collected at 590–645 nm. Laser power, gain, and exposure were kept constant across all samples. Mitophagic activity was quantified by calculating the 561/445 intensity ratio per cell using ImageJ1. For mitochondrial morphology analysis, neurons were fixed with 4% paraformaldehyde for 15 min, permeabilized with 0.1% Triton X-100 for 10 min, and blocked with 5% normal goat serum. Samples were incubated overnight at 4 °C with antiTOM20 antibody (D8T4N, Rabbit mAb; Cell Signaling Technology, #42406S), followed by Alexa Fluor 647–conjugated donkey anti-rabbit IgG (Abcam, ab150075) and DAPI (Thermo Fisher, D1306, 1 μg/mL). Images were captured using a 60× oil-immersion objective on the FV3000RS confocal microscope. Mitochondrial morphology was quantified using the Mitochondria Analyzer plugin for ImageJ 2. Image preprocessing included background subtraction, contrast enhancement (Contrast Limited Adaptive Histogram Equalization—CLAHE), and adaptive thresholding. Morphological metrics—aspect ratio, form factor, branch length, and junction count—were extracted per cell. Outliers were excluded based on automated thresholding quality control,

and batch-mode analysis was performed using optimized parameters from representative datasets.

Midbrain organoid differentiation and imaging

Midbrain organoids were generated from human iPSC lines obtained from a healthy donor (iXCells, Cat# 30HU-002) or a Parkinson's disease patient (iXCells, Cat# 30HU-003). Both lines were reprogrammed from dermal peripheral blood mononuclear cells using integration-free methods, as previously described3,4. Cells were maintained under feeder-free conditions in Human iPSC Feeder-Free Growth Medium (MD-0019) on Matrigel-coated plates and passaged with ReLeSR (STEMCELL Technologies). To induce organoid formation, dissociated iPSCs were seeded into AggreWell™800 plates and cultured using the STEMdiff™ Midbrain Organoid Differentiation Kit (STEMCELL Technologies, Cat# 100- 1096) per the manufacturer's instructions. Organoids were expanded (Days 6–25), differentiated (Days 25–43), and subsequently maintained in STEMdiff™ Neural Organoid Maintenance Medium (Cat# 100-0120) beyond Day 43. On Day 50, organoids were treated with 50 μM myriocin (Sigma-Aldrich, Cat# M1177) or vehicle (0.1% DMSO) for 48 h. After treatment, organoids were fixed in 4% paraformaldehyde (PFA) for 30 min at room temperature, cryoprotected overnight in 30% sucrose at 4 °C, embedded in optimal cutting temperature (OCT) compound, and cryosectioned at 20 μm thickness. Sections were permeabilized in 0.3% Triton X-100 for 10 min and blocked in 5% normal goat serum for 1 h at room temperature. Sections were incubated overnight at 4 °C with primary antibodies: anti-Tuj1 (BioLegend, 801213, 1:500), anti–phospho-α-synuclein (Abcam, ab184674, 1:1000), and DAPI (Thermo Fisher, D1306, 1 μg/mL). After PBS washes, sections were incubated for 1 h at room temperature with Alexa Fluor 647–conjugated anti-rabbit IgG (Abcam, ab150075) for Tuj1 labeling and PE-conjugated anti-mouse IgG ($F(ab')_2$; Cell Signaling Technology, #8887S) for phospho–α-synuclein. Whole-slide images were acquired using the FV3000RS confocal microscope. Z-stack images were collected at 20× magnification and reconstructed using maximum intensity projection. Imaging parameters were maintained constantly across experimental groups. Representative images were selected from a minimum of three organoids per condition.

Ceramide treatment in midbrain organoids and immunohistological analysis

To assess the effects of exogenous ceramide species on α-synuclein pathology, Day 50 midbrain organoids were treated with either C16 Ceramide (d18:1/16:0; Avanti Polar Lipids, Cat# 10681) or C24:1 Ceramide (d18:1/24:1(15Z); Avanti Polar Lipids, Cat# 62530) at a final concentration of 10 μM for 48 h. Ceramide stock solutions were prepared in ethanol and diluted in organoid maintenance medium immediately prior to administration. Vehicle control groups were treated with an equivalent volume of ethanol (0.1%).

Statistical analysis

Statistical analyses were performed using GraphPad Prism (version 10.0) and R (version 4.3.0). All data are presented as mean ± standard error of the mean (SEM), unless otherwise noted. Prior to the application of parametric tests, datasets were assessed for normality using the Shapiro–Wilk test. Comparisons between two groups were performed using unpaired two-tailed Student's *t*-test or Mann–Whitney U test, as deemed appropriate. For multiple group comparisons, one-way ANOVA followed by Dunnett's post hoc test was used. For behavioral analyses (e.g., open field, Y-maze), statistical comparisons were made using unpaired t-tests or one-way ANOVA, as each animal was tested once per condition. For RNA-seq data, differential expression analysis was conducted using DESeq2 with Benjamini–Hochberg correction to control the false discovery rate (FDR); genes with adjusted $p < 0.05$ and $|\log_2 \text{fold change}| > 0.58$ were considered significantly differentially expressed. Enrichment analyses (GO, KEGG, GSEA) used adjusted $p < 0.05$ as a significance threshold. For imaging-based quantification (e.g., mt-Keima ratios, aggregate counts, fluorescence intensity, morphological metrics), individual cells or organoids were designated as independent biological units (n values defined in figure legends). All image acquisition and quantification were performed under blinded conditions. Statistical significance was set at $p < 0.05$. Exact statistical tests and sample sizes (n) are indicated in the figure legends.

Ethics declarations

Human postmortem brain tissues were obtained from the Korea Brain Bank. The use of these samples was approved by the Institutional Review Board of Gwangju Institute of Science and Technology (IRB No. 20230504-BR-71-02-02). A waiver of informed consent was granted as the study utilized anonymized, postmortem biospecimens. All samples were de-identified and handled in accordance with the Declaration of Helsinki. All experimental protocols were approved by the Institutional Animal Care and Use Committee of the Gwangju Institute of Science and Technology (No. GIST-2022-041).

For detailed information on the materials and processes used in this study, please see the Supplementary Information.

Data availability

All data supporting the findings of this study can be found in the main text or supplementary materials. The sequencing data can be accessed via the Gene Expression Omnibus database (GSE298956). The statistical analyses in this study were performed using standard functions from publicly available R packages, including DESeq2 (v1.38.0), clusterProfiler (v4.4.4), ggplot2 (v3.4.2), and others as detailed in the Methods section. No proprietary or custom software was used beyond these publicly available tools. The analysis scripts are available from the corresponding author upon reasonable request.

Code availability

The statistical analyses in this study were performed using standard functions from publicly available R packages, including DESeq2 (v1.38.0), clusterProfiler (v4.4.4), ggplot2 (v3.4.2), and others as detailed in the Methods section. No proprietary or custom software was used beyond these publicly available tools. The analysis scripts are available from the corresponding author upon reasonable request.

Received: 22 August 2025; Accepted: 6 January 2026;
Published online: 21 January 2026

References

1. Aarsland, D. et al. Parkinson disease-associated cognitive impairment. *Nat. Rev. Dis. Primers* **7**, 47 (2021).
2. Rocha, E. M., De Miranda, B. & Sanders, L. H. J. N. o. d. Alpha-synuclein: Pathology, mitochondrial dysfunction and neuroinflammation in Parkinson's disease. *Neurobiol. Dis.* **109**, 249–257 (2018).
3. Iarkov, A., Barreto, G. E., Grizzell, J. A. & Echeverria, V. J. F. i. a. n. Strategies for the treatment of Parkinson's disease: beyond dopamine. *Front. Aging Neurosci.* **12**, 4 (2020).
4. Mitchell, C. L. & Kurouski, D. J. F. i. M. N. Novel strategies in Parkinson's disease treatment: a review. *Front. Mol. Neurosci.* **17**, 1431079 (2024).
5. Young, M. M., Kester, M. & Wang, H.-G. J. J. o. l. r. Sphingolipids: regulators of crosstalk between apoptosis and autophagy. *J. Lipid Res.* **54**, 5–19 (2013).
6. McInnis, J. J. et al. Unravelling neuronal and glial differences in ceramide composition, synthesis, and sensitivity to toxicity. *Commun. Biol.* **7**, 1597 (2024).
7. Jana, A., Hogan, E. L. & Pahan, K. J. J. o. t. n. s. Ceramide and neurodegeneration: susceptibility of neurons and oligodendrocytes to cell damage and death. *J. Neurol. Sci.* **278**, 5–15 (2009).
8. Mingione, A. et al. Inhibition of ceramide synthesis reduces α-synuclein proteinopathy in a cellular model of Parkinson's disease. *Int. J. Mol. Sci.* **22**, 6469 (2021).

9. Lim, J. R. et al. Ethanol-induced ceramide production causes neuronal apoptosis by increasing MCL-1S-mediated ER-mitochondria contacts. *Neurobiol. Dis.* **177**, 106009 (2023).
10. Lima, T. I. et al. Inhibiting de novo ceramide synthesis restores mitochondrial and protein homeostasis in muscle aging. *Sci. Transl. Med.* **15**, eade6509 (2023).
11. Poisson, J. et al. Safe and orally bioavailable inhibitor of serine palmitoyltransferase improves age-related sarcopenia. *ACS Pharmacol. Transl. Sci.* **8**, 203–215 (2024).
12. Kon, T., Tomiyama, M. & Wakabayashi, K. J. N. Neuropathology of Lewy body disease: clinicopathological crosstalk between typical and atypical cases. *Neuropathology* **40**, 30–39 (2020).
13. Kok, M.-Y. A. & Fu, Y. J. J. o. N. M. A new mouse tool for studying dopaminergic neurons. *J. Neurosci. Methods* **347**, 108968 (2021).
14. Nayak, S. U. et al. Chemokine CCR5 and cocaine interactions in the brain: Cocaine enhances mesolimbic CCR5 mRNA levels and produces place preference and locomotor activation that are reduced by a CCR5 antagonist. *Brain Behav. Immun.* **83**, 288–292 (2020).
15. Zhou, P., Xu, P., Yu, W., Li, H. J. J., O. O. S. & Research. MiR-206 improves intervertebral disk degeneration by targeting GJA1. *J. Orthop. Surg. Res.* **17**, 157 (2022).
16. Yang, S. et al. AZGP1 aggravates macrophage M1 polarization and pyroptosis in periodontitis. *J. Dent. Res.* **103**, 631–641 (2024).
17. Kearney, P. J. et al. Rit2 silencing in dopamine neurons drives a Parkinsonian phenotype. Preprint https://doi.org/10.1101/2023.04.26.538430 (2023).
18. Plotegher, N., Bubacco, L., Greggio, E. & Civiero, L. J. F. i. N. Ceramides in Parkinson's disease: from recent evidence to new hypotheses. *Front. Neurosci.* **13**, 330 (2019).
19. Aoki, S., Funakoshi, T., Aki, T. & Uemura, K. J. T. r. Aggregation-prone A53T mutant of α-synuclein exaggerates methamphetamine neurotoxicity in SH-SY5Y. *Cells. Prot. Role Cell. Cholest.* **9**, 2020–2029 (2022).
20. Wilkaniec, A. et al. Exogenous alpha-synuclein evoked parkin downregulation promotes mitochondrial dysfunction in neuronal cells. implications for Parkinson's disease pathology. *Front. Aging Neurosci.* **13**, 591475 (2021).
21. Giasson, B. I. et al. Neuronal α-synucleinopathy with severe movement disorder in mice expressing A53T human α-synuclein. *Neuron* **34**, 521–533 (2002).
22. Minakaki, G., Krainc, D., Burbulla, L. F. J. F. i. C. & Biology, D. The convergence of alpha-synuclein, mitochondrial, and lysosomal pathways in vulnerability of midbrain dopaminergic neurons in Parkinson's disease. *Front. Cell Dev. Biol*. **8**, 580634 (2020).
23. Biber, K. & Boddeke, E. J. F. i. c. n. Neuronal CC chemokines: the distinct roles of CCL21 and CCL2 in neuropathic pain. *Front. Cell Neurosci.* **8**, 210 (2014).
24. Lee, H.-j. et al. Regulation of habenular G-protein gamma 8 on learning and memory via modulation of the central acetylcholine system. *Mol. Psychiatry* **26**, 3737–3750 (2021).
25. Marzinke, M. A. et al. Calmin expression in embryos and the adult brain, and its regulation by all-trans retinoic acid. *Dev. Dyn.* **239**, 610–619 (2010).
26. Spielman, L. et al. Induction of the complement component C1qB in brain of transgenic mice with neuronal overexpression of human cyclooxygenase-2. *Acta Neuropathol.* **103**, 157–162 (2002).
27. Halim, D. O., Munson, M. & Gao, F.-B. J. H. G. The exocyst complex in neurological disorders. *Hum. Genet.* **142**, 1263–1270 (2023).
28. Sun, N. et al. A fluorescence-based imaging method to measure in vitro and in vivo mitophagy using mt-Keima. *Nat. Protoc.* **12**, 1576-1587 (2017).
29. Wang, S., Jin, Z., Wu, B., Morris, A. J. & Deng, P. J. J. o. L. R. Role of dietary and nutritional interventions in ceramide-associated diseases. *J. Lipid Res.* **66**, 100726 (2024).
30. Mencarelli, C. & Martinez–Martinez, P. Ceramide function in the brain: when a slight tilt is enough. *Cell. Mol. Life Sci.* **70**, 181–203 (2013).
31. Riebeling, C. & Futerman, A. H. in *Madame Curie Bioscience Database* (Landes Bioscience, 2013).
32. Schenck, M. et al. Ceramide: physiological and pathophysiological aspects. *Arch. Biochem. Biophys.* **462**, 171–175 (2007).
33. Becker, K. P., Kitatani, K., Idkowiak-Baldys, J., Bielawski, J. & Hannun, Y. A. Selective inhibition of juxtanuclear translocation of protein kinase C βII by a negative feedback mechanism involving ceramide formed from the salvage pathway. *J. Biol. Chem.* **280**, 2606–2612 (2005).
34. Poewe, W. et al. Parkinson disease. *Nat. Rev. Dis. Primers* **3**, 17013 (2017).
35. Phani, S., Gonye, G. & Iacovitti, L. VTA neurons show a potentially protective transcriptional response to MPTP. *Brain Res.* **1343**, 1–13 (2010).
36. Maingay, M., Romero-Ramos, M., Carta, M. & Kirik, D. Ventral tegmental area dopamine neurons are resistant to human mutant alpha-synuclein overexpression. *Neurobiol. Dis.* **23**, 522–532 (2006).
37. Yu, J. S. et al. Lipidomic assessment of the inhibitory effect of standardized water extract of Hydrangea serrata (Thunb.) Ser. *Leaves Adipogenes.* **16**, 1508 (2024).
38. Alderson, N. L. et al. The human FA2H gene encodes a fatty acid 2-hydroxylase. *J. Biol. Chem.* **279**, 48562–48568 (2004).
39. Xie, T. et al. Ceramide sensing by human SPT-ORMDL complex for establishing sphingolipid homeostasis. *Nat. Commun.* **14**, 3475 (2023).
40. Custodia, A. et al. Ceramide metabolism and Parkinson's disease—therapeutic targets. *Biomolecules* **11**, 945 (2021).
41. Tzou, F.-Y., Hornemann, T., Yeh, J.-Y. & Huang, S.-Y. The pathophysiological role of dihydroceramide desaturase in the nervous system. *Prog. Lipid Res.* **91**, 101236 (2023).
42. Levy, M. & Futerman, A. H. Mammalian ceramide synthases. *IUBMB Life* **62**, 347–356 (2010).
43. Rai, M. et al. Analysis of proteostasis during aging with western blot of detergent-soluble and insoluble protein fractions. *STAR Protoc.* **2**, 100628 (2021).
44. Lee, B. R. & Kamitani, T. Improved immunodetection of endogenous α-synuclein. *PloS ONE* **6**, e23939 (2011).
45. Laurila, P.-P. et al. Inhibition of sphingolipid de novo synthesis counteracts muscular dystrophy. *Sci. Adv.* **8**, eabh4423 (2022).

Acknowledgements

This research was supported by Bio & Medical Technology Development Program of the NRF funded by the Korean government (Grant No.: RS-2024-00440824), Korea Health Technology R&D Project through the Korea Health Industry Development Institute, funded by the Ministry of Health & Welfare, Republic of Korea (Grant No.: RS-2024-00439685), Korean ARPA-H Project through the Korea Health Industry Development Institute, funded by the Ministry of Health & Welfare, Republic of Korea (Grant No.: RS-2024-00507256), the National Research Foundation of Korea (NRF) funded by the Korean government (Grant No.: RS-2025-25424683), and National Research Council of Science & Technology (NST) grant by the Korean government (Grant No.: CAP23021-000). Additional funding was provided by Korea Basic Science Institute (National research Facilities and Equipment Center) grant funded by the Ministry of Education (Grant No.: 2023R1A6C101A045). The funders played no role in study design, data collection, analysis and interpretation of data, or the writing of this manuscript. Human brain tissue was provided by the Korea Brain Bank Network (CNUHB, AMCB, KNUHB) operated through the National Brain Bank Project funded by the Ministry of Science and ICT. We would like to express our sincerest gratitude to the participating brain banks for providing these human brain research resources.

Author contributions

D.P., G.L., H.R., and C.-M.O. designed and supervised this study. E.L. and M.P. performed in vitro and in vivo experiments. E.L. and M.P. generated the figures. E.L. and C.-M.O. drafted the manuscript. D.P., G.L., and C.-M.O. edited the manuscript. All authors have discussed the results and approved the manuscript.

Competing interests

The authors declare no competing interests.

Additional information

Supplementary information The online version contains supplementary material available at https://doi.org/10.1038/s41531-026-01263-5.

Correspondence and requests for materials should be addressed to Dohyun Park, Gakyung Lee or Chang-Myung Oh.